King Saud University

Arabian Journal of Chemistry

www.ksu.edu.sa
www.sciencedirect.com

ORIGINAL ARTICLE

Study on the mechanism of removing fluoride from wastewater by oxalic acid modified aluminum ash-carbon slag-carbon black doped composite

Yuanchuan Ren [a,b], Minjie He [a,b], Guangfei Qu [a,b,*], Nanqi Ren [c], Ping Ning [a,b], Yuyi Yang [a,b], Xiuping Chen [a,b], Zuoliang Wang [a,b], Yan Hu [a,b]

[a] *Faculty of Environmental Science and Engineering, Kunming University of Science and Technology, Kunming, Yunnan 650500, China*
[b] *National Regional Engineering Research Center-NCW, Kunming, Yunnan 650500, China*
[c] *School of Environment, Harbin Institute of Technology, Harbin 150090, China*

Abstract   In this study, SAA@CS-CB(aluminum-ash carbide slag carbon black doped composite) was prepared by sintering method and modified by impregnation with oxalic acid to obtain SAA@CS-CB$_{oa}$. Fluoride adsorption experiments were carried out using this composite as adsorbent. With increasing pH values, the adsorption amount of fluoride decreases in the range of 2–11. The pseudo second order equation and Langmuir model were fit to the experimental data, and the adsorption of fluoride by SAA@CS-CB$_{oa}$ exhibited spontaneous and endothermic characteristics. When PO_4^{3-}, CO_3^{2-}, SO_4^{2-}, Cl^-, NO_3^-, Br^- and HCO_3^- anions were individually or combined in solution, the adsorbents exhibited higher fluoride selectivity and sensitivity, while PO_4^{3-} and CO_3^{2-} weakened the adsorption of fluoride in solution in the same way regardless of the presence of the other 5 anions. The results of SEM, EDS, XRD and FTIR characterizations showed that the mechanism of fluoride adsorption and removal by SAA@CS-CB$_{oa}$ included the combined effects of electrostatic attraction, surface coordination precipitation and ion exchange. SAA@CS-CB$_{oa}$ is an effective composite material for water adsorption of fluoride, and still has an excellent performance of cyclic regeneration after 10 times adsorption desorption. This study provides a new approach for the utilization of fluoride removal resources for industrial solid waste resource recycling.

* Corresponding author.
  E-mail address: qgflab@sina.com (G. Qu).
Peer review under responsibility of King Saud University.

Production and hosting by Elsevier
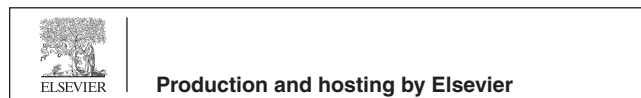
1. Introduction

Aluminum ash, which is a derivative of the aluminum smelting process (Chang et al., 2022), usually consists of metallic aluminum, aluminum oxides, and oxides of multiple alloying elements, is one of the major hazardous solid wastes generated in the aluminum electrolysis industry. These contain large amounts of aluminum compounds, sodium compounds, silicon oxides, etc., and have a large potential for recovery (Zhang et al., 2022). Aluminum ash is divided into primary aluminum ash and secondary aluminum ash (SAA), and secondary aluminum ash (Ni et al., 2022) there is currently no mature comprehensive utilization process, and there is a serious threat of metal pollution to the environment. Therefore, the harmless and efficient disposal of aluminum ash has received wide attention by the industry, and in-depth studies have been carried out from several perspectives. The main technologies include the recovery of alumina, the preparation of aqueous aluminum chloride net, various kinds of refractory materials, building materials and road materials, the recovery of fluoride and chlorine salts, etc. (Yang et al., 2022). Preparation of aluminum chloride netwater by secondary aluminum ash the process is using pyrolysis synergistic harmless disposal technology, and calcium aluminate netwater (Maach et al., 2021) synthesized by using secondary aluminum ash as raw material has better water purification effect, but there are more impurities, which need to be continuously improved.

Carbide slag (Hu et al., 2021) is a typical industrial solid waste, a strong alkaline waste residue produced by the hydrolysis of aragonite in the process of industrial production of polyvinyl chloride, and about 1.2 t is produced per ton of aragonite, and about 32.4 million t is produced per year, the main component of which is $Ca(OH)_2$. Due to the high alkalinity of carbide slag (CS) and containing some harmful components such as hydrogen sulfide that are difficult to treat, the comprehensive utilization rate of carbide slag is relatively low (Zhu et al., 2022). At present, the main disposal method of carbide slag is solid–liquid separation, which is finally treated by landfill or waste, which causes a great waste of resources (Wang et al., 2021). An ad libitum stack of carbide slag can occupy a large amount of land, and the long-term compost penetration of carbide slag can cause the saline alkalization of land and contaminate water resources, severely damaging the ecological environment, crisis to the surrounding areas of residents' life and physical health (Li et al., 2022). Therefore, how to realize the secondary utilization of industrial waste is one of the current issues that need to be addressed (Yang et al., 2021). The carbide slag is rich in calcium resources and has many advantages, such as good dispersion of particles, large specific surface area, large pore structure, and low thermal decomposition temperature, which can be used as a secondary resource to replace limestone in the building materials industry and is widely used as an inner wall paint, thermal insulation and so on (Gong et al., 2022). The main resource-based applications of carbide slag in environmental protection are the production of desulfurization agents, treatment of acidic wastewater and so on (Miao et al., 2022).

Carbon black (CB) is a product derived from the incomplete combustion or thermal decomposition of carbonaceous materials (coal, natural gas, heavy oil, fuel oil, etc.) under air deficient conditions (Feng et al., 2021). There has been extensive research as reinforcement of rubber, filler of plastic, pigments, etc. (Cheng et al., 2021). Not difficult to find after studying the structure and properties of carbon black, its large specific surface area and special structure and surface properties, are very latent in adsorption applications (Wang et al., 2021). Relative to the extensive research on carbon materials such as activated carbon (Xia et al., 2021), carbon nanotubes (Tong et al., 2021), there is little research on carbon black as an adsorbent. Based on the large specific surface area and surface chemistry of carbon black, its use as an adsorbent for the treatment of organic and inorganic pollutants in water bodies has been some reported. For example: chemical modification of carbon black and adsorption of arsenic in water after modification (Schaller et al., 2018), waste carbon black as adsorbent to treat diphenylamine production wastewater (Leventis et al., 2004), adsorption properties of pyrolytic carbon black for Cr (VI) from aqueous solutions (Wang et al., 2019), Carbon black treatment of spent caustic liquor after desulfation and CO_2 removal from natural gas (Wang, 2002) and so on.

However, up to now, studies on the utilization of secondary aluminum ash, carbide slag as well as carbon black for the preparation of composites for fluoride degra dation are still rare. Therefore, secondary aluminum ash, carbide slag as well as carbon black sintering were selected to prepare composites for fluoride adsorption in this study. In addition, we also investigated the effects of pH and coexisting ions on fluoride adsorption. The mechanism involved in the fluoride adsorption process was revealed by bet, SEM, EDS, XRD and FTIR. This study provides a valuable reference for the long-term treatment of the disposal of industrial solid waste. At the same time, it provides an effective route and theoretical support for developing low-cost, safe and high-performance adsorbents.

2. Materials and methods

2.1. Materials

NaF, NaBr, NaCl, NaNO$_3$, Na$_2$SO$_4$, Na$_2$CO$_3$, NaHCO$_3$, Na$_3$PO$_4$, HCl, NaOH and oxalic acid were purchased from China Tianjin Zhiyuan Fine Chemical Co., ltd. (analytical grade). The secondary aluminum ash (SAA), carbide slag (CS) and carbon black (CB) were provided by Yunnan Coal Chemical Industry Group Co., ltd.

2.2. Preparation of SAA@CS-CB

Certain amounts of secondary aluminum ash, carbide slag as well as carbon black were weighed and put into a vacuum drying oven and dried at 60 ℃ for 12 h. Each group after drying was sieved through a 100 mesh sieve. Weigh 30 g of secondary aluminum ash, carbide slag as well as carbon black with a mass ratio of 1:1:1 and place the crucible into a muffle furnace, which is set up with a programmed temperature of 5 °C per minute and raised to 700 °C for 4 h. The samples were removed for treatment with room temperature water. Then put into the vacuum drying box to adjust the temperature 60 ℃ for 12 h, remove cooled to room temperature, and grind to obtain SAA@CS-CB.

2.3. Modified of SAA@CS-CB

10 g of SAA@CS-CB was weighed and placed in a triangular flask, to which 100 ml of oxalic acid (wt 2 %) was added and magnetically stirred at room temperature for 12 h. Then the supernatant was filtered off and the filter residue was cleaned with distilled water three times and placed at 60 ℃ for 12 h under vacuum drying. SAA@CS-CB$_{oa}$ was finally obtained by grinding with a mortar.

2.4. Characterization of materials

The compositions of the crystal structure were clarified by X-ray diffraction (XRD) (Rigaku ultimate 4, RIGAKU Co., Japan). The surface morphology of materials was determined by scanning electron microscope (SEM) (JSM-5800, Japan JEOL), and element contents and their distribution were identified through Energy dispersive X-ray spectroscopy (EDS). The specific surface area of the materials were measured by automatic specific surface analyzer(BET) (ASAP 2020, Micromeritics Co., U.S.A) calculations. In addition, fourier transform infrared spectroscopy (FTIR) (IRTracer-100, SHIMADZU Co., Japan) spectra analysis was used to investigate the surface functional groups, recording in the range of 500–4000 cm^{-1}.

2.5. Batch adsorption experiments

First, the fluoride ion solution used in this study was prepared by dissolving sodium fluoride in ultrapure water to produce a fluoride ion containing stock solution (1000 mg·L^{-1}). Next, the main concentration of the solution used for testing fluoride removal was 100 mg·L^{-1}. Then, the conditions of these main adsorption experiments were performed using 25 mg of adsorbent at a pH of 2.0 for 1 h. The removal efficiency of fluoride was calculated as follows:

$$q_t = (\frac{C_o - C_t}{m})V \quad (1)$$

Where C_o was the original fluoride concentration (mg·L^{-1}), C_t was the concentration of fluoride at time.

Different values of pH were tested using hydrochloric acid and sodium hydroxide as modifiers from pH = 2–11. To better understand the adsorption process, different initial concentrations ranging from 10 mg·L^{-1} to 1000 mg·L^{-1} were investigated as adsorption isotherms at different temperatures (30 °C, 40 °C, 50 °C). The obtained data attempted to fit the Langmuir model and Freundlich model. These models were shown as follows:

$$\frac{C_e}{q_e} = \frac{1}{q_{max} \cdot K_L} + \frac{C_e}{q_{max}} \quad (2)$$

$$\ln q_e = \ln K_F + \frac{\ln C_e}{n} \quad (3)$$

Where C_e is the fluoride concentration at equilibrium (mg L^{-1}); q_{max} is the adsorption amount required to form a complete monolayer (mg/g); K_L and K_F represent diverse isotherm constants; $1/n$ is an empirical parameter related to the adsorption intensity. The different reaction time changed from 0.5 min to 360 min was studied as adsorption kinetics at different temperatures (30 °C, 40 °C, 50 °C), too. Pseudo-first order kinetic model and Pseudo-second order kinetic model were used to know the adsorption kinetics. These models were exhibited in these equations.

$$Pseudo - first - order \, equation : \ln(q_e - q_t) = \ln q_e - k_1 t \quad (4)$$

$$Pseudosecond - order : \frac{t}{q_t} = \frac{t}{q_e} + \frac{1}{k_2 q_e^2} \quad (5)$$

$$Elovich \, equation : q_t = \frac{\ln(\alpha\beta)}{\beta} + \frac{\ln t}{\beta} \quad (6)$$

$$Intra - particle \, diffusion : q_t = k_i t^{0.5} + C_i \quad (7)$$

Where q_e and q_t are the adsorption amounts of fluoride at equilibrium and after time (t; min), respectively (mg·g^{-1}); k_1, k_2, k_i, α and β stand for rate constants of diverse kinetics; C_i is a parameter describing the boundary layer thickness.

Enthalpy change (ΔH^o), entropy change (ΔS^o) and free energy change (ΔG^o) were computed with the following equations:

$$\Delta G^o = -RT \ln K$$
$$\ln K = \frac{\Delta S^o}{R} - \frac{\Delta H^o}{RT} \quad (8)$$

Where R is the gas constant (8.314 J K^{-1} mol^{-1}), T is the temperature (K) and K represents the adsorption constant.

Different concentrations of negative ions were added into fluoride solutions (0, 0.25, 0.5, 1, 3, 5, 10, 20, 50, 100, 200 mol·L^{-1}). The negative ions included HCO_3^-, Br^-, NO_3^-, Cl^-, CO_3^{2-}, SO_4^{2-}, PO_4^{3-}demonstrated the effect of coexisting anions. F^- adsorbed on the material can be desorbed by acid, alkali, salt and other substances. In order to ensure the adsorption performance of adsorbent after desorption, the selection of desorption agent depends largely on the content of –OH. In this experiment, NaOH solution rich in carboxyl and weak acid was selected as the desorption agent. The materials were investigated in ten cycles about regeneration performance. SAA@CS-CB (original), SAA@CS-CB (sintering) and SAA@CS-CB$_{oa}$ were both applied in a batch of adsorption experiments to judge this performance of modification. In this study, we use ion chromatography to determine the concentration of fluoride in aqueous solution. all experiments were repeated three times to find the average value.

3. Results and discussion

3.1. Characterization of material

The properties and structures of the synthesized materials have been studied using characterization techniques. SEM and EDS analysis of the materials are shown in Fig. 1. Before sintering, the particle size was larger and ranged from 0.55 μm around that and the particles were agglomerated, the main elements were o, C, Al, Ca (Fig. 1a). After sintering at 700 °C, the particles were clearly found to be porous and grape like in distribution(Zhao et al., 2021); with an average size between 0.11 μm around with little change in elemental composition (Fig. 1b). After modification by immersion of oxalic acid (Fig. 1c), a large number of fine particles appeared, resulting in the surface of SAA@CS-CB becoming rough (Zhang et al., 2022); and the particle size increased to 0.16 μm. At the same time, the content of O to C increased obviously and the percentage contents
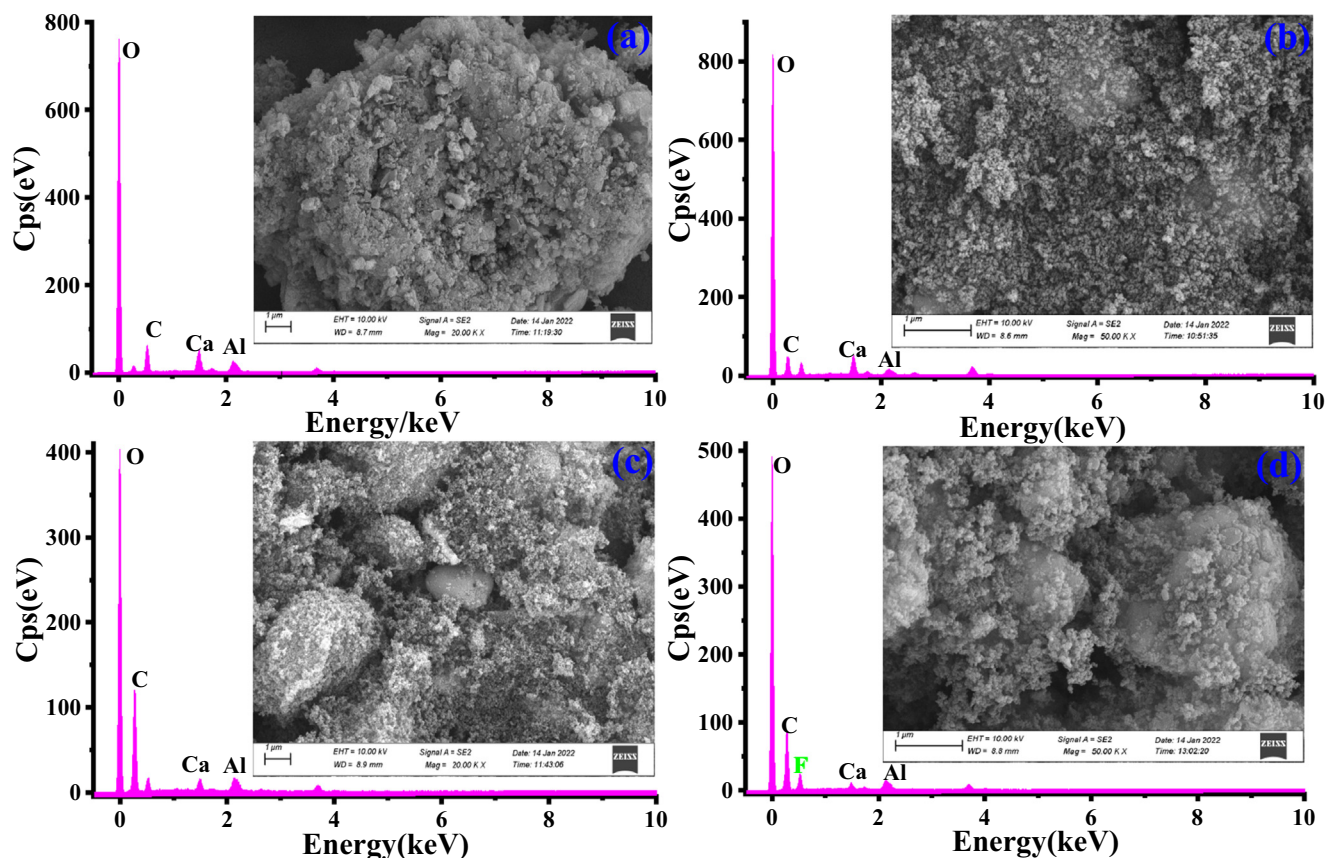
Fig. 1 SEM images and EDS spectra of adsorbent with different treatment: (a) original, (b) sintering, (c) modification, (d) after adsorption.

of Al and Ca decreased. After fluoride adsorption, the size increased to 0.20 μ m. Its surface roughness increases (Zhang et al., 2022); and the occurrence of elemental fluoride indicates that fluoride adsorbs on the surface of the material (Fig. 1d).

The BET results of the materials under different treatment conditions are shown in Table 1. After being determined by BET analyzer, the specific surface areas of SAA@CS-CB (before sintering), SAA@CS-CB (after sintering), SAA@CS-CB$_{oa}$ and SAA@CS-CB$_{oa}$ (after adsorption) were 621.32, 775.16, 843.12 and 584.14 m$^2 \cdot$g^{-1}. The pore volumes were 0.27, 0.32, 0.35 and 0.26 cm$^3 \cdot$g^{-1}, and the single site adsorption average pore diameters were 18.00, 18.62, 19.04, and 17.05 nm, respectively. It is not hard to find out that after modified by sintering and oxalic acid, the specific surface area was raised by 24.28 % and 35.70 %, respectively, and the pore volume and average pore size were also increased, which indicated that using sintering and oxalic acid to modify the physical properties of materials could provide a possibility for the next

adsorption experiments. After fluoride adsorption, the specific surface area decreases to 584.14 m$^2 \cdot$g^{-1}, and the corresponding pore volume and average pore size also become significantly smaller (Baskar et al., 2022).

Fig. 2a shows the FTIR spectra of SAA@CS-CB (original), SAA@CS-CB (sintering), SAA@CS-CB$_{oa}$ and SAA@CS-CB$_{oa}$ (after adsorption). It was found that the FTIR spectra of the various phases were phase similar. The absorption peaks around 3440, 2928 and 678 cm^{-1} in the figure come from the stretching vibration of O—H, C—H and C—C bonds respectively (Tao et al., 2020). The absorption peak around 1641 cm^{-1} is the result of asymmetric stretching of C=O bond (Li et al., 2022). The absorption peak around 1431 cm^{-1} is attributed to C—C symmetric stretching vibration (Li et al., 2022). After sintering and modification, the intensity of the absorption peak is weakened, and the peak area is small. After adsorption, a new absorption peak appeared at 1167 cm^{-1}, indicating the formation of Al-F bond (Zheng et al., 2021).

Table 1 Specific surface area of SAA@CS-CB (original), SAA@CS-CB (sintering), SAA@CS-CB$_{oa}$ and SAA@CS-CB$_{oa}$ (after adsorption).

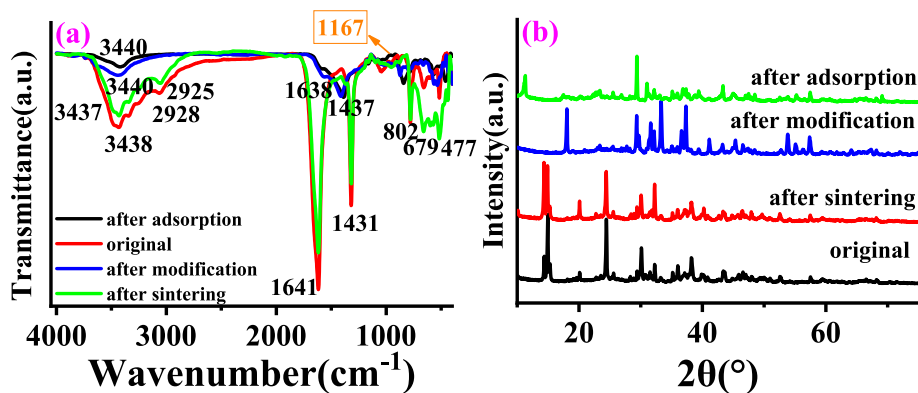| Adsorbent	BET surface area (m$^2 \cdot$g^{-1})	Pore volume (cm$^3 \cdot$g^{-1})	Average pore diameter (nm)
SAA@CS-CB (original)	621.32	0.27	18.00
SAA@CS-CB (sintering)	775.16	0.32	18.62
SAA@CS-CB$_{oa}$	843.12	0.35	19.04
SAA@CS-CB$_{oa}$ (after adsorption)	584.14	0.26	17.05

Fig. 2   The FTIR (a) and XRD (b) spectra of adsorbent with different treatment.

The broad band at 400–900 cm^{-1} and peaks at 1437 cm^{-1} could be attributed to the stretching vibrations of Al—O and Al=O bonds, respectively (Kundu et al., 2017).

Fig. 2b compares the XRD patterns of SAA@CS-CB (original), SAA@CS-CB (sintering), SAA@CS-CB$_{oa}$ and SAA@CS-CB$_{oa}$ (after adsorption). Among them, the main diffraction peaks before and after sintering of the materials were similar, it is worth mentioning that before sintering, the main components of the materials were aluminum oxide, aluminum nitride, and calcium hydroxide. After sintering, one diffraction peak ($2\theta = 20°$), and the strength increased, indicating that sintering made more oxygen-containing functional groups (Zhang et al., 2020). Although there is a low-intensity broad peak when $2\theta = 30°$, it does not affect the crystal structure of the material. This illustrates that the structure of the material is completely crystalline (Jiang et al., 2015). After modification with oxalic acid, the main peaks were right shifted and new crystals were formed, indicating the deposition of oxalic acid on the surface of the material. It further illustrates that the modification of oxalic acid is feasible. After adsorption, the diffraction peaks ($2\theta = 20°$, $2\theta = 30$–$40°$ and $2\theta = 55°$) disappeared, indicating that removal of fluoride ions may be the formation of complexes (Al-F, Ca-F).

3.2. Effect of dosage and pH

The exploration of the effect of adsorbent(SAA@CS-CB: aluminum-ash carbide slag carbon black doped composite) dosage versus pH on the adsorption performance is shown in
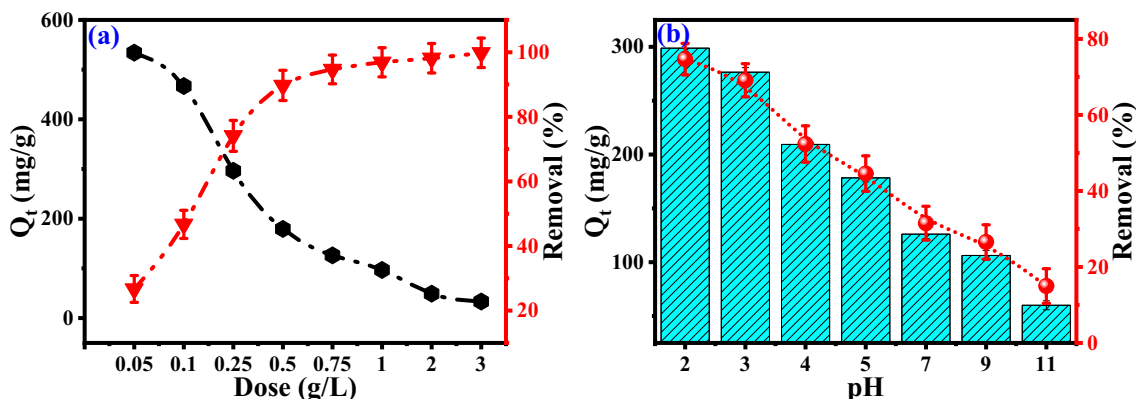
Fig. 3. It can be obviously found in Fig. 3a that the removal rate of fluoride from the solution kept increasing with the increasing adsorbent dosage. This is due to the constant total amount of fluoride in the solution, while the increasing number of adsorbents makes more and more adsorption sites (Zhang et al., 2022) available for fluoride ion adsorption, thus increasing the removal rate. However, with the increase of adsorbent dosage, the adsorption capacity is continuously getting smaller, especially after the dosage exceeds 0.25 g·L^{-1}, the adsorbent capacity drops sharply. As can be seen, the increased adsorbent dosage of one taste is not the most economically feasible and only causes waste of resources. Therefore, it is particularly important to choose the smallest adsorbent dosage to obtain the maximum adsorption capacity and removal efficiency. The best results were obtained at a dose of 0.25 g·L^{-1}, at which point the adsorption capacity was 296.44 mg·g^{-1} and the removal efficiency was 74.11 %.

As shown in Fig. 3b, the greater the initial concentration of the solution, the greater the effect of pH on the adsorbent's (SAA@CS-CB, which was original) equilibrium adsorption capacity for fluoride.When the pH of the solution is 2, the surface of the material is positively charged, and the fluoride in the solution mainly exists in the F$^-$ form, leading to the generation of electrostatic attraction between them (Zhang et al., 2022); contributing to the adsorption reaction progress. The adsorption capacity at this point was the best at 298.76 mg·g^{-1}, and the removal efficiency was 74.69 %. This can be explained by measuring the pH$_{pzc}$ of SAA@CS-CB. The pH$_{pzc}$ of the material sample is 7.6. It is reported that the pH$_{pzc}$ range of

Fig. 3   Effect of dosage (a) and pH (b) on fluoride removal by the adsorbent.

activated alumina is 6.2 ∼ 8.9.38 (Kumari et al., 2019). The effect of pH on the adsorption capacity is due to the electrostatic or coulomb interaction between the material surface and F⁻ ions in the aqueous solution (Kumari et al., 2020). According to the value of pH_{pzc}, the surface of the material is slightly alkaline, forming an Al-OH bond. As the pH value of the solution decreases, that is, pH < pH_{pzc}, the material surface is positively charged, so F⁻ ions are adsorbed on the material surface (Chen et al., 2022). When the pH is much lower than pH_{pzc}, the electrostatic attraction conducive to the adsorption of F⁻ ions becomes higher (Tao et al., 2020). With the increase of pH above pH_{pzc}, that is, pH > pH_{pzc}, the adsorption of F⁻ ions on the material decreases because F⁻ ions are adsorbed and repelled from F⁻ ions on the surface of negatively charged hydrogen and oxygen ions (Shin et al., 2021). F⁻ ion and hydroxide ion compete to combine on the surface of the adsorbent, thus reducing the adsorption of fluoride ion (Kumari et al., 2020). As described in previous work,
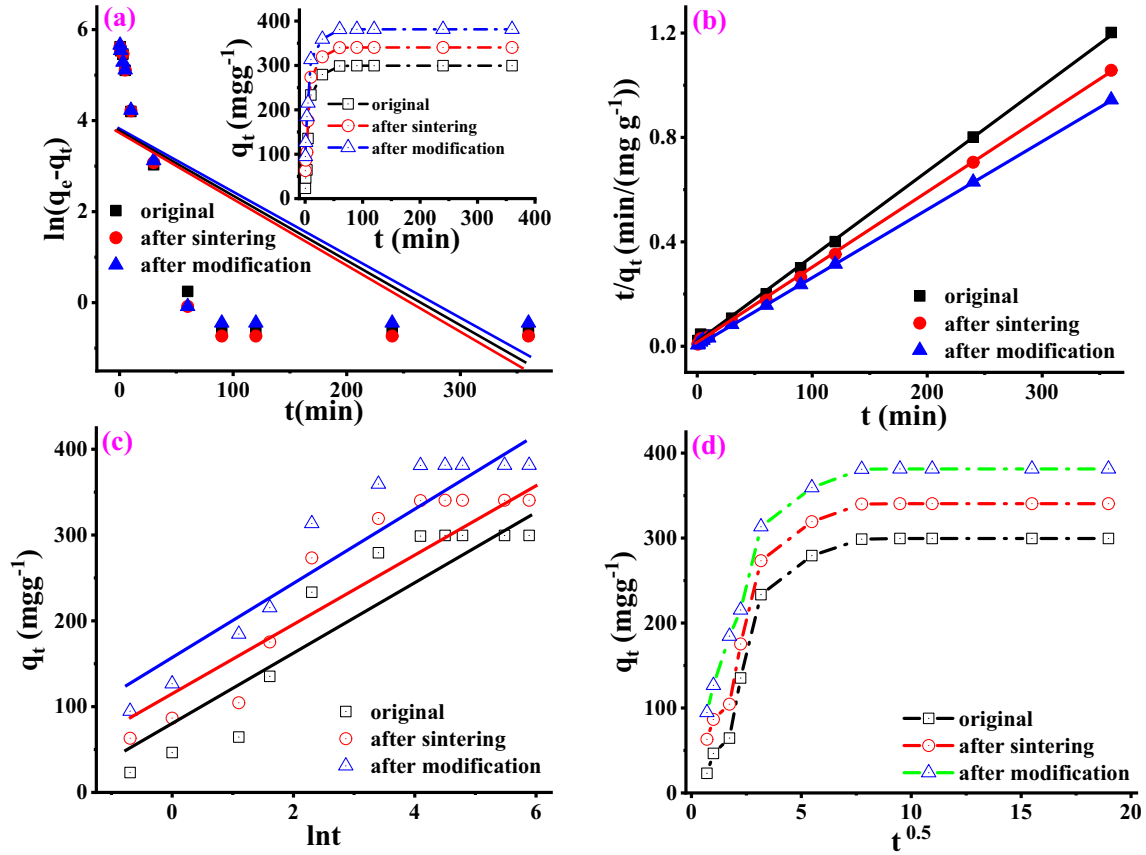

Fig. 4 Adsorption kinetics of fluoride on adsorbent: (a) pseudo-first-order, (b) pseudo-second-order, (c) elovich equation, (d) intra-particle diffusion.

Table 2 Kinetic parameters for SAA@CS-CB (original), SAA@CS-CB (sintering) and SAA@CS-CB$_{oa}$.

		SAA@CS-CB (original)	SAA@CS-CB (sintering)	SAA@CS-CB$_{oa}$
$q_{e(exp)}$/mg·g^{-1}		298.72	340.08	381.08
Pseudo-first-order	k_1/min^{-1}	0.02	0.02	0.02
	$q_{e(cal)}$/mg·g^{-1}	52.97	51.38	51.89
	R^2	0.5753	0.5657	0.5532
Pseudo-second-order	k_2/g·(mg·min)$^{-1}$	7.03*10^{-4}	9.78*10^{-4}	1.28*10^{-3}
	$q_{e(cal)}$/mg·g^{-1}	303.03	344.83	374.62
	R^2	1.00	1.00	1.00
Elovich equation	α	176.58	397.04	1028.81
	β	0.02	0.02	0.02
	R^2	0.89	0.90	0.91
Intra-particle diffusion	k_1	14.56	14.67	14.31
	C_1	105.09	145.06	190.8
	R^2	0.61	0.61	0.61

materials do not undergo hydrolysis at acidic pH, which minimizes electrostatic repulsion and increases adsorption capacity (Du et al., 2022).

3.3. *Adsorption kinetics*

To evaluate the effect of contact time on the adsorption process of fluoride ions on the materials, we performed kinetic experiments, and the results are shown in Fig. 4. The maximum adsorption capacity was achieved at 60 min after the adsorption process, at which point the adsorption capacities were 298.72 $mg \cdot g^{-1}$, 340.08 $mg \cdot g^{-1}$ and 381.08 $mg \cdot g^{-1}$ for 74.68 %, 85.02 % and 95.27 %, respectively. It is clearly seen that sintering and modification treatment enhanced the adsorption capacity by 41.36 $mg \cdot g^{-1}$ and 82.36 $mg \cdot g^{-1}$ and the removal efficiency by 13.85 % and 27.57 %, respectively. This indicates that after sintering and modification with oxalic acid, the adsorption properties of SAA@CS-CB can be improved step by step.

Fig. 4 and Table 2 are the data fitting of adsorption kinetics models such as pseudo first order, pseudo second order, elovich equation and intra particle diffusion along with related calculations. It was found by the data fitting of the model that the calculated adsorption capacities were basically consistent with the best ones obtained in the experiments, and the correlation coefficients R^2 were all 1.00. Therefore, we can state that this adsorption process mainly satisfies the pseudo second order kinetics (Li et al., 2022). It can also be found that after sintering and modification with oxalic acid, the adsorption rate of SAA@CS-CB increases gradually upon the adsorption of fluoride ions, from $7.03*10^{-4}$ to $9.78*10^{-4}$, and finally reaches $1.28*10^{-3}$ $k_2 \cdot g \cdot (mg \cdot min)^{-1}$. This indicates that after sintering and oxalic acid modification, the adsorption sites on the surface of SAA@CS-CB increase gradually, which enables more fluoride ions to adsorb on the surface of the material (Xia et al., 2022); thereby increasing the adsorption capacity. The pseudo second order kinetic model suggests that the adsorption of the main fluoride ions is mainly accomplished by covalent binding (Lin et al., 2022) via sharing or electron transfer. Therefore, whether chemisorption can occur and how fast and slow the interaction rate depends on the number of active sites on the surface of the material (Zhang et al., 2022).

3.4. *Isotherm and thermodynamics study*

The effect of initial concentration of fluoride from 0.5 to 1000 $mg \cdot L^{-1}$ on the adsorbent was investigated at different temperature conditions and the results are shown in Fig. 5a. At room temperature, with the increase of initial fluoride concentration, the adsorption capacity increased rapidly and reached the maximum value (296.08, 341.08 and 381.36 $mg \cdot g^{-1}$). At this time, the initial fluorine concentration was 100 $mg \cdot L^{-1}$. This shows that the adsorption capacity of SAA@CS-CB is satisfactory over most of the adsorbents reported (Ma et al., 2022). When the initial fluoride ion concentration continued to increase, the adsorption capacity tended to be stable. While the adsorption capacity of SAA@CS-CB (original), SAA@CS-CB (sintering) and SAA@CS-CB$_{oa}$ for fluoride ions increased gradually as the temperature increased from 25 to 35 and 45 °C. Moreover, in many existing studies, higher q_{max} appears often because
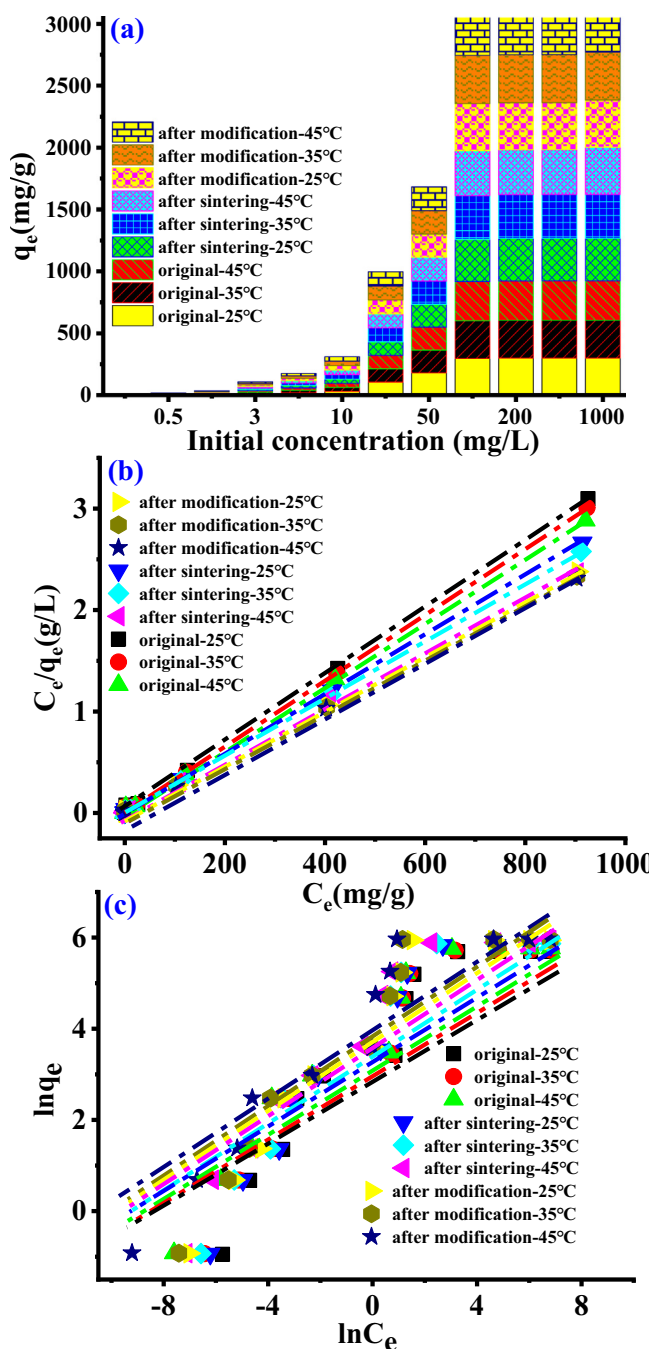

Fig. 5 Effect of initial concentration (a) and adsorption isotherm models of fluoride on adsorbent:the Langmuir model (b), the Freundlich model (c).

they set a higher initial concentration of fluoride (Ma et al., 2022); while in this study, SAA@CS-CB also show more significant q_{max} at low fluoride concentrations. This can indicate that SAA@CS-CB has the potential to remove fluoride due to its good adsorption capacity, high speed and conditional advantages. We adopted Langmuir and Freundlich models to conduct adsorption isotherm fitting to the experimental data (Fig. 5b and c). Fig. 5b shows that all points are evenly distributed on both sides of the straight line, whereas the points in Fig. 5c are scattered more distantly on both sides

of the line, indicating that the fit to the data is more consistent with the Langmuir equation (Wang et al., 2022). This may be due to the different adsorption sites of the surface adsorption energy of the material, indicating that oxalic acid is relative to the unmodified material. The adsorption energy of the material surface to the main hydroxyl sites such as Al-OH is different (Abdelrahman and Al-Farraj, 2022). Meanwhile, it is shown in Table 3 that the values of R^2 (1.00) under Langmuir fitting are all higher than those (0.90) under Freundlich fitting, further indicating that the Langmuir equation can better describe this adsorption process. It was implied that monolayer fluoride adsorption occurred on the adsorbent surface and had energetically identical adsorption sites (Zhou et al., 2022).

To investigate the effect of temperature on the fluoride adsorption properties of SAA@CS-CB and explore the spontaneity and driving force of the adsorption process, thermodynamic calculations were performed in Eqs. (8). The calculation results are shown in Table 4. The ΔG^o was negative at all temperatures and decreased with increasing temperature, demonstrating that the adsorption process was spontaneous (Li et al., 2022). Also illustrated from the side that an increase in temperature is beneficial for better fluoride adsorption because it can better desolve ions in solution (Qu et al., 2022). More importantly, ΔH^o and ΔS^o all had positive values indicating that the adsorption was an endothermic process. With the increase of the experimental temperature, the value of K_F also increases, indicating that the temperature can promote the adsorption process, which further proves that the adsorption process is an endothermic reaction (Shin et al., 2021). The greater the value of K_F, the stronger the combina-

tion ability reflected (Kumari et al., 2020). Therefore, the combination of fluorine and SAA@CS-CB$_{oa}$ is much easier than the original materials. The adsorption capacity of SAA@CS-CB (original), SAA@CS-CB (sintering) and SAA@CS-CB$_{oa}$ increase with increasing temperature, more illustrating this adsorption process.

3.5. Effect of coexisting ions and cycle times on adsorption performance

To evaluate the influence of coexisting ions (PO_4^{3-}, CO_3^{2-}, SO_4^{2-}, Cl^-, NO_3^-, Br^- and HCO_3^-) on the adsorption process of fluoride ions on the materials, we performed anion interference experiments, and the results are shown in Fig. 6a. It can be found that SAA@CS-CB$_{oa}$ was all highly selected F^-, SO_4^{2-}, Cl^-, NO_3^-, Br^- and HCO_3^- have a negligible effect on the adsorption. Specifically, the presence of CO_3^{2-} has little effect on the adsorption capacity, only reducing by 3.56 %. However, the presence of PO_4^{3-} had a significant effect, and with increasing concentrations, the adsorption capacities of SAA@CS-CB$_{oa}$ decreased by 84.75 %. On the one hand, the hydration radii of PO_4^{3-} and CO_3^{2-} are close to those of F^-, thus hindering the diffusion of F^- to the adsorbent surface. On the other hand, it may be due to the competition between $-OH$ and F^- generated from PO_4^{3-} and CO_3^{2-} hydrolysis (Chen et al., 2022); as evidenced from the increase of solution pH(3.65) after adsorption.
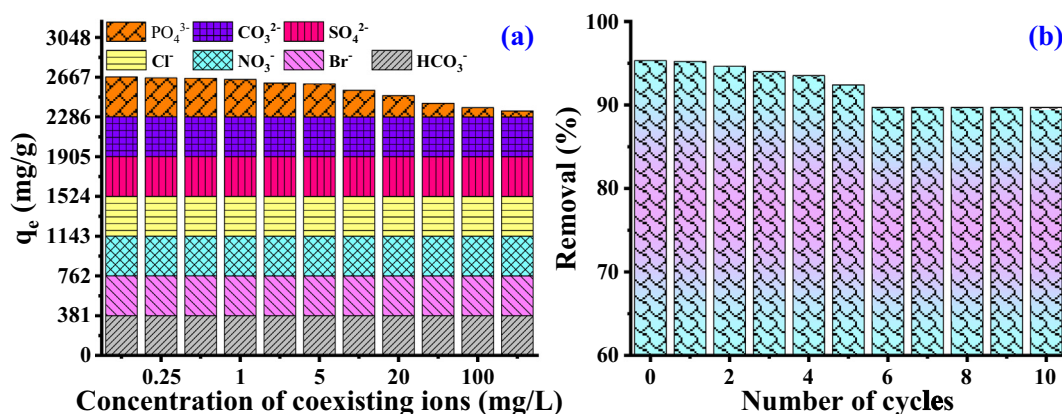
The adsorption performance of an adsorbent after desorption strongly depends on the content of $-OH$ in the desorbent. We selected NaOH with a mass concentration of 5 % as the

Table 3 Isotherm parameters for the Langmuir model at different temperatures about SAA@CS-CB (original), SAA@CS-CB (sintering) and SAA@CS-CB$_{oa}$.

		pH2.0, dosage of adsorbent (0.25 g·L^{-1})		
		SAA@CS-CB (original)	SAA@CS-CB (sintering)	SAA@CS-CB$_{oa}$
Freundlich model				
298.15 K	K_F	26.97	32.70	40.75
	1/n	0.51	0.51	0.50
	R^2	0.88	0.89	0.88
308.15 K	K_F	30.94	37.39	44.99
	1/n	0.49	0.50	0.48
	R^2	0.89	0.88	0.88
318.15 K	K_F	36.81	44.10	54.62
	1/n	0.46	0.48	0.44
	R^2	0.91	0.89	0.89
Langmuir model				
298.15 K	$q_{e(exp)}$	296.08	341.08	381.36
	q_{max}	303.03	344.83	384.62
	K_L	0.24	0.33	0.39
	R^2	1.00	1.00	1.00
308.15 K	$q_{e(exp)}$	305.76	353.28	387.40
	q_{max}	312.50	357.14	384.62
	K_L	0.30	0.45	0.45
	R^2	1.00	1.00	1.00
318.15 K	$q_{e(exp)}$	316.36	362.20	389.84
	q_{max}	322.58	384.62	384.62
	K_L	0.34	0.31	0.58
	R^2	1.00	1.00	1.00

Table 4 Standard thermodynamic parameters for adsorption of fluoride ions on SAA@CS-CB (original), SAA@CS-CB (sintering), SAA@CS-CB$_{oa}$.

	T/K	$\Delta G^o/(kJ\cdot mol^{-1})$	$\Delta H^o/(kJ\cdot mol^{-1})$	$\Delta S^o/(J\cdot K^{-1}\cdot mol^{-1})$
SAA@CS-CB (original)	298.15 K	−6.03	11.16	0.06
	308.15 K	−6.57		
	318.15 K	−7.19		
SAA@CS-CB (sintering)	298.15 K	−7.79	19.88	0.09
	308.15 K	−8.73		
	318.15 K	−9.64		
SAA@CS-CB$_{oa}$	298.15 K	−10.92	24.87	0.12
	308.15 K	−12.33		
	318.15 K	−13.31		

Fig. 6 Effect of coexisting anions (a) and cyclic adsorption-regeneration runs (b) on the adsorption of fluoride about the adsorbent after modification.

desorption agent (Huang et al., 2020). Therefore, we performed adsorption desorption 10 cycle experiments to explore the adsorbent's recycling performance, and the results are shown in Fig. 6b. As the number of cycles increased, the adsorption capacity of the material slowly decreased, and it remained at 89.71 % of the initial adsorption capacity even for the 10th cycle. In summary, SAA@CS-CB$_{oa}$ has excellent recovery properties.

3.6. Mechanism of adsorption

The fluoride removal mechanism of SAA@CS-CB$_{oa}$ was clearly shown in Fig. 7. (1) Electrostatic attraction (Alhassan et al., 2022): SAA@CS-CB$_{oa}$ adsorbed F$^-$ to the surface by electrostatic attraction; (2) coordination (Huang et al., 2020): the complexes react with Al and Ca to form Al-F and Ca-F complexes on the surface of the material; (3) sedimentation (Kong et al., 2020): F$^-$ adsorbed on the surface of SAA@CS-CB$_{oa}$ react with calcium carbonate to generate CaF$_2$ precipitate; (4) ion exchange (Yang et al., 2022): the production of the M−F complex releases the hydroxide and forms stable AlO-F; CaO-F, and CO-F compounds. Therefore, the mechanism of fluoride adsorption and removal by SAA@CS-CB$_{oa}$ includes the combined effects of electrostatic attraction, coor-

dination, sedimentation and ion exchange. The chemical reactions involved are as follows:
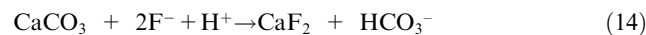
Electrostatic attraction:

$$AlOOHH^+ + F^- \rightarrow AlOOHHF \tag{9}$$

$$CaOOHH^+ + F^- \rightarrow CaOOHHF \tag{10}$$

$$HOOCCOOH + F^- \rightarrow HOOCCOOHF \tag{11}$$

Coordination:

$$AlOOH + F^- \rightarrow F\text{-}AlOOH \tag{12}$$

$$CaOOH + F^- \rightarrow F\text{-}CaOOH \tag{13}$$

Sedimentation:

$$CaCO_3 + 2F^- + H^+ \rightarrow CaF_2 + HCO_3^- \tag{14}$$

Ion exchange:

$$AlOOH + F^- \rightarrow AlO\text{-}F + OH \tag{15}$$

$$HOOCCOOH + F^- \rightarrow HOOCCOF + OH \; 16 CaOOH$$
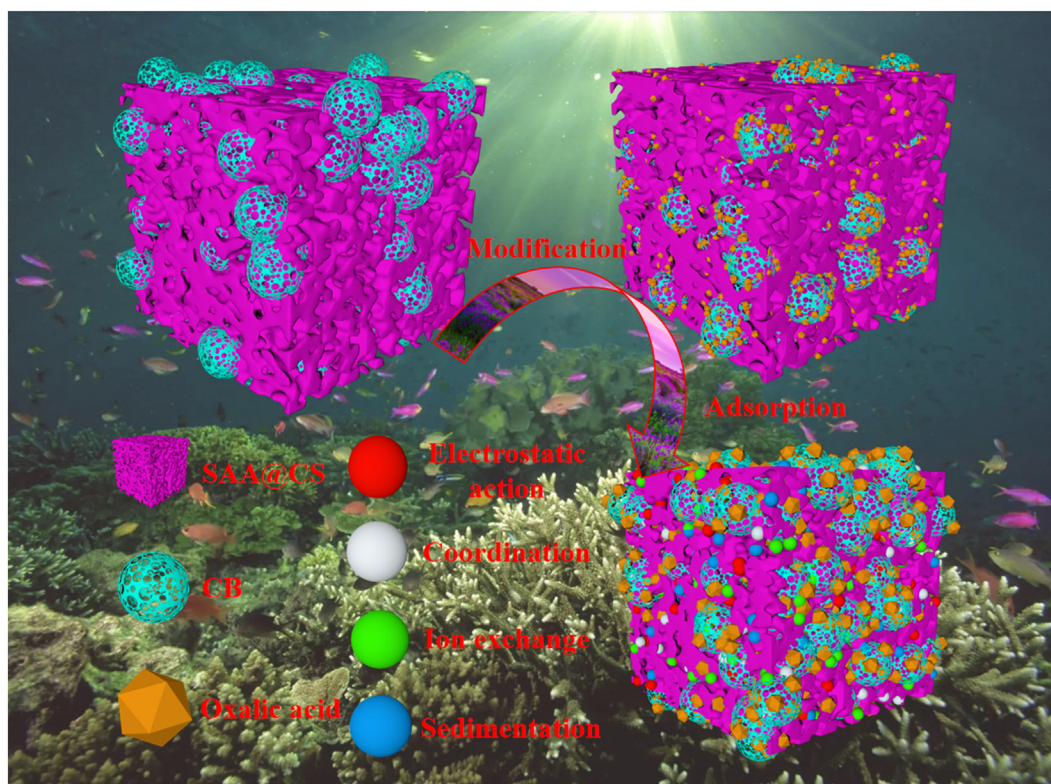$$+ F^- \rightarrow CaO - F + OH$$

$$\tag{17}$$

Fig. 7   The mechanism of fluoride adsorption by SAA@CS-CB$_{oa}$.

4. Conclusion

In this study, SAA@CS-CB was prepared by sintering method and modified by impregnation with oxalic acid to obtain SAA@CS-CB$_{oa}$. Fluoride adsorption experiments were carried out using this composite as adsorbent. With increasing pH values, the adsorption amount of fluoride decreases in the range of 2–11. The pseudo second order equation and Langmuir model were fit to the experimental data, and the adsorption of fluoride by SAA@CS-CB$_{oa}$ exhibited spontaneous and endothermic characteristics. When PO_4^{3-}, CO_3^{2-}, SO_4^{2-}, Cl^-, NO_3^-, Br^- and HCO_3^- anions were individually or combined in solution, the adsorbents exhibited higher fluoride selectivity and sensitivity, while PO_4^{3-} and CO_3^{2-} weakened the adsorption of fluoride in solution in the same way regardless of the presence of the other 5 anions. The results of SEM, EDS, XRD and FTIR characterizations showed that the mechanism of fluoride adsorption and removal by SAA@CS-CB$_{oa}$ included the combined effects of electrostatic attraction, surface coordination precipitation and ion exchange. SAA@CS-CB$_{oa}$ is an effective composite material for water adsorption of fluoride, and still has an excellent performance of cyclic regeneration after 10 times adsorption desorption. The synthesis of composite materials opens up a new way for the development of adsorption materials. Therefore, SAA@CS-CB$_{oa}$ may be a viable adsorption material to help remove fluoride in wastewater. In addition, through in-depth discussion on the adsorption of fluoride by composite materials prepared from industrial solid waste, researchers will be encouraged to develop new ideas on process/product improvement to further improve the removal potential of adsorbent.

Declaration of competing interest

The authors declare that they have no known competing financial interests or personal relationships that could have appeared to influence the work reported in this paper.

Acknowledgements

Author Agreement

We confirm that the manuscript has been read and approved by all named authors and that there are no other persons who satisfied the criteria for authorship but are not listed. We further confirm that the order of authors listed in the manuscript has been approved by all of us.

Signed by all authors as follows: Yuanchuan Ren, Minjie He, Guangfei Qu*, Nanqi Ren, Ping Ning, Yuyi Yang, Xiuping Chen, Zuoliang Wang, Yan Hu.

References

Abdelrahman, E.A., Al-Farraj, E.S., 2022. Facile synthesis and characterizations of mixed metal oxide nanoparticles for the efficient photocatalytic degradation of Rhodamine B and Congo Red dyes. Nanomaterials 12.

Alhassan, S.I., Wang, H.Y., He, Y.J., Yan, L.J., Jiang, Y.X., Wu, B.C., Wang, T., Gang, H.Y., Huang, L., Jin, L.F., Chen, Y.S., 2022. Fluoride remediation from on-site wastewater using optimized bauxite nanocomposite (Bx-Ce-La@500): Synthesis maximization, and mechanism of F- removal. J. Hazard. Mater. 430.

Baskar, A.V., Bolan, N., Hoang, S.A., Sooriyakumar, P., Kumar, M., Singh, L., Jasemizad, T., Padhye, L.P., Singh, G., Vinu, A., Sarkar, B., Kirkham, M.B., Rinklebe, J., Wang, S.S., Wang, H.L., Balasubramanian, R., Siddique, K.H.M., 2022. Recovery, regeneration and sustainable management of spent adsorbents from wastewater treatment streams: a review. Sci. Total Environ. 822.

Chang, Z.Y., Long, G.C., Xie, Y.J., Zhou, J.L., 2022. Pozzolanic reactivity of aluminum-rich sewage sludge ash: Influence of calcination process and effect of calcination products on cement hydration. Constr. Build. Mater. 318.

Chen, C.L., Shih, Y.J., Su, J.F., Chen, K.L., Huang, C.P., 2022. Mesoporous zirconium pyrophosphate for the adsorption of fluoride from dilute aqueous solutions. Chem. Eng. J. 427.

Chen, J.B., Yang, R.J., Zhang, Z.Y., Wu, D.Y., 2022. Removal of fluoride from water using aluminum hydroxide-loaded zeolite synthesized from coal fly ash. J. Hazard. Mater. 421.

Cheng, H.B., Sun, X.L., Huang, B.Q., Xiao, L.R., Chen, Q.H., Cao, C.L., Qian, Q.R., 2021. Endowing acceptable mechanical properties of segregated conductive polymer composites with enhanced filler-matrix interfacial interactions by incorporating high specific surface area nanosized carbon black. Nanomaterials 11.

Du, M., Zhang, Y.Y., Wang, Z.Y., Lv, M.R., Tang, A.Q., Yu, Y., Qu, X., Chen, Z.Q., Wen, Q.X., Li, A., 2022. Insight into the synthesis and adsorption mechanism of adsorbents for efficient phosphate removal: exploration from synthesis to modification. Chem. Eng. J. 442.

Feng, D.D., Shang, Q., Dong, H.M., Zhang, Y., Wang, Z.L., Li, D., Xie, M., Wei, Q.Y., Zhao, Y.J., Sun, S.Z., 2021. Catalytic mechanism of Na on coal pyrolysis-derived carbon black formation: Experiment and DFT simulation. Fuel Process. Technol. 224.

Gong, X.Z., Zhang, T., Zhang, J.Q., Wang, Z., Liu, J.H., Cao, J.W., Wang, C.A., 2022. Recycling and utilization of calcium carbide slag-current status and new opportunities. Renew. Sustain. Energy Rev. 159.

Hu, Y.P., Wu, S.M., Li, Y.J., Zhao, J.L., Lu, S.J., 2021. H2S removal performance of Ca3Al2O6-stabilized carbide slag from CO2 capture cycles using calcium looping. Fuel Process. Technol. 218.

Huang, L., Yang, Z.H., He, Y.J., Chai, L.Y., Yang, W.C., Deng, H.Y., Wang, H.Y., Chen, Y.S., Crittenden, J., 2020. Adsorption mechanism for removing different species of fluoride by designing of core-shell boehmite. J. Hazard. Mater. 394.

Jiang, X.X., Liu, G.R., Wang, M., Liu, W.B., Tang, C., Li, L., Zheng, M.H., 2015. Case study of polychlorinated naphthalene emissions and factors influencing emission variations in secondary aluminum production. J. Hazard. Mater. 286, 545–552.

Kong, L.C., Tian, Y., Pang, Z., Huang, X.H., Li, M., Li, N., Zhang, J., Zuo, W., Li, J.J., 2020. Needle-like Mg-La bimetal oxide nanocomposites derived from periclase and lanthanum for cost-effective phosphate and fluoride removal: Characterization, performance and mechanism. Chem. Eng. J. 382.

Kumari, U., Behera, S.K., Meikap, B.C., 2019. A novel acid modified alumina adsorbent with enhanced defluoridation property: kinetics, isotherm study and applicability on industrial wastewater. J. Hazard. Mater. 365, 868–882.

Kumari, U., Behera, S.K., Siddiqi, H., Meikap, B.C., 2020. Facile method to synthesize efficient adsorbent from alumina by nitric acid activation: batch scale defluoridation, kinetics, isotherm studies and implementation on industrial wastewater treatment. J. Hazard. Mater. 381.

Kundu, S., Chowdhury, I.H., Sinha, P.K., Naskar, M.K., 2017. Effect of organic acid-modified mesoporous alumina toward fluoride ions removal from water. J. Chem. Eng. Data 62, 2067–2074.

Leventis, H.C., Streeter, I., Wildgoose, G.G., Lawrence, N.S., Jiang, L., Jones, T.G.J., Compton, R.G., 2004. Derivatised carbon powder electrodes: reagentless pH sensors. Talanta 63, 1039–1051.

Li, S.R., Chen, X., Li, M.J., Xue, C., Long, Y.H., Liu, W.H., Cao, Z.H., Tong, X.Q., Huang, W.L., Liu, D.F., 2022. Hollow Co3S4 polyhedron decorated with interlayer-expanded MoS2 nanosheets for efficient tetracycline removal from aqueous solution. Chem. Eng. J. 441.

Li, Y., Gao, L.H., Zhan, W.L., He, Z.J., Zhang, J.H., Hou, X.M., 2022. Synergetic utilization of microwave-modified fly ash and carbide slag for simultaneous desulfurization and denitrification. J. Clean. Prod. 349.

Li, J.C., Guo, J.Y., Dai, H.J., 2022. Probing dissolved CO2(aq) in aqueous solutions for CO2 electroreduction and storage. Sci. Adv. 8.

Li, Y., Koopal, L.K., Tan, W.F., Chai, Y.J., Chen, Y., Wu, C.Y., Tang, X., 2022. Effect of humic acid on lysozyme interaction with montmorillonite and kaolinite. Sci. Total Environ. 834.

Li, H., Li, C., Budarin, V.L., Clark, J.H., North, M., Wang, J.X., Wu, X., 2022. Synthesis, characterisation and carbon dioxide capture capacities of hierarchically porous Starbons(R). Green Chem. 24, 1545–1560.

Lin, J.W., Li, L.C., Ma, L.S., Hu, Y.Y., Zhao, C., Wei, L.T., Zheng, G.M., Liu, S.G., Shan, Q., Zhao, H.Y., Yin, Y., 2022. Carbonized poly(dopamine)@Co-0 composites for the high-efficient removal of sulfamethoxazole: role of direct electron-transfer and adsorption. Chem. Eng. J. 445.

Ma, X.F., Zhao, S.Y., Tian, Z.W., Duan, G.G., Pan, H.Y., Yue, Y.Y., Li, S.S., Jian, S.J., Yang, W.S., Liu, K.M., He, S.J., Jiang, S.H., 2022. MOFs meet wood: reusable magnetic hydrophilic composites toward efficient water treatment with super-high dye adsorption capacity at high dye concentration. Chem. Eng. J. 446.

Maach, N., Georgin, J.F., Berger, S., Pommay, J., 2021. Chemical mechanisms and kinetic modeling of calcium aluminate cements hydration in diluted systems: Role of aluminium hydroxide formation. Cem. Concr. Res. 143.

Miao, E.D., Zheng, X.F., Xiong, Z., Zhao, Y.C., Zhang, J.Y., 2022. Kinetic modeling of direct aqueous mineral carbonation using carbide slag in a stirred tank reactor. Fuel 315.

Ni, H.J., Wu, W.Y., Lv, S.S., Wang, X.X., Tang, W.J., 2022. Formulation of non-fired bricks made from secondary aluminum ash. Coatings 12.

Qu, Y., Qin, L., Liu, X.G., Yang, Y.Z., 2022. Magnetic Fe3O4/ZIF-8 composite as an effective and recyclable adsorbent for phenol adsorption from wastewater. Sep. Purif. Technol. 294.

Schaller, J., Wang, J.J., Islam, M.R., Planer-Friedrich, B., 2018. Black carbon yields highest nutrient and lowest arsenic release when using rice residuals in paddy soils. Sci. Rep. 8.

Shin, E., Dreisinger, D.B., Burns, A.D., 2021. Removal of fluoride from sodium sulfate brine by zirconium pre-loaded chelating resins with amino-methyl phosphonic acid functionality. Desalination 505.

Tao, W., Zhong, H., Pan, X.B., Wang, P., Wang, H.Y., Huang, L., 2020. Removal of fluoride from wastewater solution using Ce-AlOOH with oxalic acid as modification. J. Hazard. Mater. 384.

Tong, Z.W., Yuan, Y.F., Yin, S.M., Wang, B.X., Zhu, M., Guo, S.Y., 2021. Preparation and high-performance lithium storage of intimately coupled MnO_2 nanosheets@carbon nanotube-in-nanotube. Sustain. Mater. Technol. 29.

Wang, S., 2002. Application of complex flocculants harness the waste water of produce cotton fiber. Environ. Chem. 21, 292–295.

Wang, W., Li, S., Lin, W., Li, Y., Zhang, L., Han, J., 2019. Removal of Cr(VI) from solution by carbon black/zero valence iron composites coupled with metal reducing bacteria. Ecol. Environ. Sci. 28, 2062–2069.

Wang, N., Mao, M., Mao, G.Y., Yin, J.B., He, R.X., Zhou, H.C., Li, N., Liu, Q.S., Zhi, K.D., 2021. Investigation on carbide slag catalytic effect of Mongolian bituminous coal steam gasification process. Chemosphere 264.

Wang, H., Qiu, C., Song, Y., Bian, S., Wang, Q., Chen, Y., Fang, C., 2022. Adsorption of tetracycline and Cd(II) on polystyrene and polyethylene terephthalate microplastics with ultraviolet and hydrogen peroxide aging treatment. Sci. Total Environ. 845, 157109.

Wang, S.W., Vallejos-Burgos, F., Furuse, A., Yoshikawa, Y., Tanaka, H., Kaneko, K., 2021. The subtracting pore effect method for an accurate and reliable surface area determination of porous carbons. Carbon 175, 77–86.

Xia, C.F., Huang, H.H., Liang, D.R., Xie, Y., Kong, F.P., Yang, Q. H., Fu, J.X., Dou, Z.W., Zhang, Q., Meng, Z.L., 2022. Adsorption of tetracycline hydrochloride on layered double hydroxide loaded carbon nanotubes and site energy distribution analysis. Chem. Eng. J. 443.

Xia, J.S., Mahandra, H., Ghahreman, A., 2021. Efficient gold recovery from cyanide solution using magnetic activated carbon. Acs Appl. Mater. Interfaces 13, 47642–47649.

Yang, J., Liu, S.Y., Ma, L.P., 2021. Thermodynamic analysis of hydrogen production from carbide slag used as oxygen carrier, hydrogen carrier and in-situ carbon capture agent during the gasification of lignite. Energ. Conver. Manage. 244.

Yang, J.J., Sun, H.J., Peng, T.J., Zeng, L., Chao, L., 2022. Separation of alumina from aluminum-rich coal fly ash using NaOH molten salt calcination and hydrochemical process. Clean Techn. Environ. Policy 24, 1507–1519.

Yang, Y., Wang, Y.N., Zheng, C.Y., Lin, H.W., Xu, R.K., Zhu, H.Q., Bao, L.L., Xu, X.H., 2022. Lanthanum carbonate grafted ZSM-5 for superior phosphate uptake: investigation of the growth and adsorption mechanism. Chem. Eng. J. 430.

Zhang, G.G., Fang, Y.G., Wang, Y.D., Liu, L.J., Mei, D.C., Ma, F. Q., Meng, Y.J., Dong, H.X., Zhang, C.H., 2022. Synthesis of amino acid modified MIL-101 and efficient uranium adsorption from water. J. Mol. Liq. 349.

Zhang, X.R., Guo, J.G., Zhou, L.J., 2022. Experimental and theoretical investigation on the adsorption properties of benzene on graphene surface: influence of pH and edge effects. Chem. Eng. J. 440.

Zhang, J.J., Liu, B., Zhao, S.Z., Shen, H.L., Liu, J., Zhang, S.G., 2020. Preparation and characterization of glass ceramic foams based on municipal solid waste incineration ashes using secondary aluminum ash as foaming agent. Constr. Build. Mater. 262.

Zhang, J.J., Liu, B., Shen, H.L., Wen, Q., Liu, Y., Liu, J., Zhang, S.E., 2022. Theoretical and experimental on the thermodynamic, kinetic and phase evolution characteristics of secondary aluminum ash. J. Mater. Res. Technol.-Jmr&T 19, 3857–3866.

Zhang, G.H., Xue, P., Wei, J., Zhang, Y.H., Zhao, L., Gao, J.S., Xu, C.M., 2022. Competitive adsorption mechanism of thiophene with diethyl sulfide in Y zeolite: displacement and migration. Chem. Eng. J. 435.

Zhao, X., Zhao, H.H., Huang, X.R., Wang, L., Liu, F.H., Hu, X.F., Li, J.T., Zhang, G.B., Ji, P.H., 2021. Effect and mechanisms of synthesis conditions on the cadmium adsorption capacity of modified fly ash. Ecotoxicol. Environ. Saf. 223.

Zheng, D.W., Huang, T.W., Xu, B., Zhou, X., Mao, Y.F., Zhong, L., Gao, B., Wang, D.J., 2021. 3D printing of n-Al/Polytetrafluoroethylene-based energy composites with excellent combustion stability. Adv. Eng. Mater. 23.

Zhou, S., Yin, J., Ma, Q., Baihetiyaer, B., Sun, J.X., Zhang, Y., Jiang, Y.J., Wang, J., Yin, X.Q., 2022. Montmorillonite-reduced graphene oxide composite aerogel (M-rGO): a green adsorbent for the dynamic removal of cadmium and methylene blue from wastewater. Sep. Purif. Technol. 296.

Zhu, G.Y., Meng, Z.H., Li, S.P., Zhao, L.W., Qi, F., Li, Z.B., He, S., Li, H.Q., 2022. High efficiency desulfurization behavior by the sustainable low carbon utilization of carbide slag. Process Saf. Environ. Prot. 159, 809–818.